Lab on a Chip

ROYAL SOCIETY OF CHEMISTRY

PAPER

View Article Online
View Journal | View Issue

Check for updates

Cite this: *Lab Chip*, 2025, **25**, 3766

Received 25th September 2024,
Accepted 20th June 2025

DOI: 10.1039/d4lc00799a

rsc.li/loc

In-Petri-dish acoustic vortex tweezers†

Teng Li,[a] Yingshan Du,[b] Bowen Cai,[a] Michael R. Brooks,[c] Chongpeng Qiu,[a] Zhide Wang,[a] Jiali Li,[a] Luyu Bo,[a] Y. Albert Pan[c] and Zhenhua Tian*[a]

Acoustic tweezers, with the capability to manipulate tiny objects without physical contact, hold substantial potential for biomedical and biological research. However, current acoustic tweezers platforms face challenges in precise, selective, and multi-degree-of-freedom (multi-DoF) manipulation of objects in Petri dishes, making it difficult to integrate them into typical laboratory workflows. This paper presents an acoustic vortex tweezers platform that enables contactless, precise, multi-DoF, and multifunctional manipulation of micro-to-millimeter-scale objects within a Petri dish. The platform features an acoustic holography-based module, which uses a holographic lens to transform acoustic waves and generate a focused acoustic vortex beam. This beam carries sufficient energy to propagate through a Petri dish's bottom wall, creating a ring-shape intensity field for trapping tiny objects. Using lenses encoded with different topological charge numbers, vortex beams with varying diameters can be generated, allowing for trapping various-sized objects. Additionally, in combination with a 3-DoF linear motion module, our integrated platform enables high-resolution translation of acoustically trapped objects along complex paths. We experimentally demonstrated our platform's diverse capabilities, including concentrating micro-objects, trapping flowing micro-objects to create an agglomerate, translating a microparticle and an agglomerate along complex paths, as well as trapping, rotating and translating a zebrafish larva in horizontal and vertical postures. With these capabilities, we expect our in-Petri-dish acoustic vortex tweezers to emerge as a valuable tool for the contactless, high-resolution, programmable handling of tiny biomaterials in biomedical and biological research.

Introduction

Technologies enabling high-precision, contactless manipulation of tiny objects—such as optical,[1,2] electrical,[3,4] magnetic,[5,6] and acoustic tweezers[7–18]—have shown great potential in biological, chemical, environmental, and biomedical research. Among these, acoustic tweezers have been continuously attracting increasing attention in recent years due to their notable features. Unlike other technologies, acoustic manipulation doesn't rely on the target object's optical, electrical, or magnetic properties; instead, it depends on the object's universal material properties, such as compressibility and acoustic impedance,[19–21] ensuring the ability to manipulate objects with various material properties. Acoustic tweezers can manipulate objects ranging in size from tens of nanometers to several millimeters such as exosomes,[22–25] cells,[26–31] worms,[32] zebrafish larvae,[33–35] microrobots,[36–39] *etc.* Additionally, acoustic tweezers can manipulate objects shielded by biological barriers such as real tissue and bone,[40–42] as acoustic waves can transmit through these materials.

Acoustics-based contactless object manipulation has seen significant advancements in recent years and been successfully applied to a wide range of applications, such as patterning cells for bio-fabrication,[27–29] concentrating biomarkers for signal enhancement,[43–45] separating platelets from whole blood,[24,46,47] *in vivo* manipulation of bioparticles,[48–51] *etc.* Most acoustic tweezers devices use one or multiple pairs of parallelly arranged transducers, such as bulk acoustic wave and surface acoustic wave transducers, to generate standing acoustic waves for contactless object manipulation. For example, using a pair of transducers, standing acoustic waves with parallel-line-like intensity fields can be generated to align cells for fabricating anisotropic tissues and separating bioparticles of different sizes.[52,53] Using two pairs of transducers arranged orthogonally, small particles can be organized into rectangular-grid-like patterns,[50,54] and acoustic devices with more transducer pairs

---

[a] *Department of Mechanical Engineering, Virginia Polytechnic Institute and State University, Blacksburg, VA, 24060, USA. E-mail: tianz@vt.edu*
[b] *Department of Biomedical Engineering and Science, Virginia Polytechnic Institute and State University, Blacksburg, VA, 24060, USA*
[c] *Fralin Biomedical Research Institute, Viginia Polytechnic Institute and State University, Roanoke, VA, 24016, USA*

† Electronic supplementary information (ESI) available. See DOI: **https://doi.org/10.1039/d4lc00799a**

arranged in different orientations allows for increasing the particle pattern complexity,[55] as well as offering more achievable patterns of particles.

In addition to using standing acoustic waves, the acoustic holography mechanism, which can generate complex holographic acoustic fields through the interference of phase-modulated acoustic waves, has been introduced to develop acoustic tweezers.[11,56,57] By using a three-dimensional (3D) printed holographic lens, whose thickness profile is encoded with a high-resolution phase profile, incident acoustic waves can be modulated to carry that phase profile as they transmit through the lens. The interference of phase-modulated acoustic waves further creates a desired holographic acoustic field, which depends on the phase profile encoded in the lens. This approach has been demonstrated to generate complex acoustic fields, allowing particles to be arranged into highly complex patterns (*e.g.*, patterns depicting letters).[58–60] Instead of using lenses to modulate acoustic waves, by depositing Archimedes spiral-shaped electrodes on a piezoelectric wafer, holographic transducers have recently been developed to generate an acoustic vortex, enabling the selective trapping and translation of single microparticles.[61,62] Despite significant progress in the development of acoustic tweezers devices, there is still a lack of a platform that allows for contactless, precise, and multi-DoF manipulation of micro-to-millimeter-scale objects in a Petri dish, one of the most commonly used supplies in biological and biomedical laboratories. We believe that such a platform, capable of in-Petri-dish object manipulation, can be easily integrated into biomedical laboratory workflows, thus benefiting researchers in the biological and biomedical communities.

To fill the technological gap, this study presents an in-Petri-dish acoustic vortex tweezers platform that enables contactless, precise, multi-DoF, and multifunctional manipulation of micro-to-millimeter-scale objects in liquid within a Petri dish. This platform takes advantage of an acoustic holography-based module, which uses a 3D printed holographic lens to transform incident acoustic waves into a focused acoustic vortex beam, with the majority of energy confined in the beam while carrying orbital angular momentum.[63,64] This beam has sufficient energy to transmit through the bottom wall of a Petri dish and create a ring-shaped acoustic potential well, which functions as an invisible end effector to trap a small object inside the well, as well as concentrate micro-objects to create an agglomerate. Moreover, the orbital angular momentum of the acoustic vortex beam can apply torque to the trapped object, enabling rotational manipulation of the object.[65,66] Furthermore, our acoustic vortex tweezers platform, which integrates the acoustic vortex module and a 3-DoF linear motion stage, allows for in-Petri-dish translation of the acoustically trapped object along customized high-resolution paths within a plane parallel to the Petri dish's bottom wall. As the holographic lens is interchangeable, different lenses can be used to generate focused vortex beams with different topological charge numbers, thus creating potential wells with various diameters for trapping and manipulating objects of different sizes. Additionally, our acoustic vortex tweezers platform can be operated under an upright fluorescence microscope, thereby allowing for monitoring fluorescent signal changes during acoustic manipulation.

To validate our in-Petri-dish acoustic vortex tweezers platform, a series of experiments was performed. We measured the output acoustic fields, confirming the generation of acoustic vortex beams with different potential well diameters when using different holographic lenses. We also successfully demonstrated multiple manipulation capabilities in a Petri dish, including (i) concentrating tiny objects by shrinking an acoustic potential well, (ii) capturing flowing micro-objects to create an agglomerate with a controlled diameter, (iii) translating a micro-object and a cluster of micro-objects along complex paths, as well as (iv) trapping, rotating and translating a zebrafish larva in horizontal and vertical postures.

Results

Design and mechanism of in-Petri-dish acoustic vortex tweezers

Our acoustic vortex tweezers platform illustrated in Fig. 1(a) is composed of two key modules: (i) a holography-based acoustic vortex device for generating a focused acoustic vortex beam that can transmit through a Petri dish's bottom wall to create an in-Petri-dish acoustic potential well for trapping tiny objects (*e.g.*, microparticles, cells, and zebrafish larva) preloaded in the Petri dish, as well as (ii) a high-resolution, 3-DoF linear motion stage for translating the acoustic vortex device attached on the stage, thus precisely moving the tiny objects trapped by the focused acoustic vortex beam's center potential well within a plane parallel to the Petri dish's bottom wall. Additionally, as shown by a photo (Fig. 1(c)) of the experimental setup, the acoustic vortex device can be integrated with an upright fluorescence microscope, enabling the capture of brightfield and fluorescence microscopic images during the acoustic vortex-based manipulation of microscale objects.

The schematic in Fig. 1(b) illustrates the generation of a focused acoustic vortex beam using our acoustic vortex device. The device has a compact design that combines a circular, plate-type piezoelectric transducer and an additively manufactured holographic lens with an ultrasound coupling gel in between. The piezoelectric transducer generates pressure acoustic waves, by exciting the transducer using a sinusoidal voltage signal at a frequency matching the transducer's thickness-mode resonance frequency. The holographic lens has a spatially varying thickness profile $h(\mathbf{x})$ to transform the acoustic waves generated from the circular piezoelectric transducer. As the generated acoustic waves transmit through the holographic lens, they will be spatially modulated, thus carrying the phase shift information $\Delta\phi(\mathbf{x}) = (k_\mathrm{f} - k_\mathrm{lens})h(\mathbf{x}) - k_\mathrm{f}h_\mathrm{max}$, where h_max is the maximum thickness

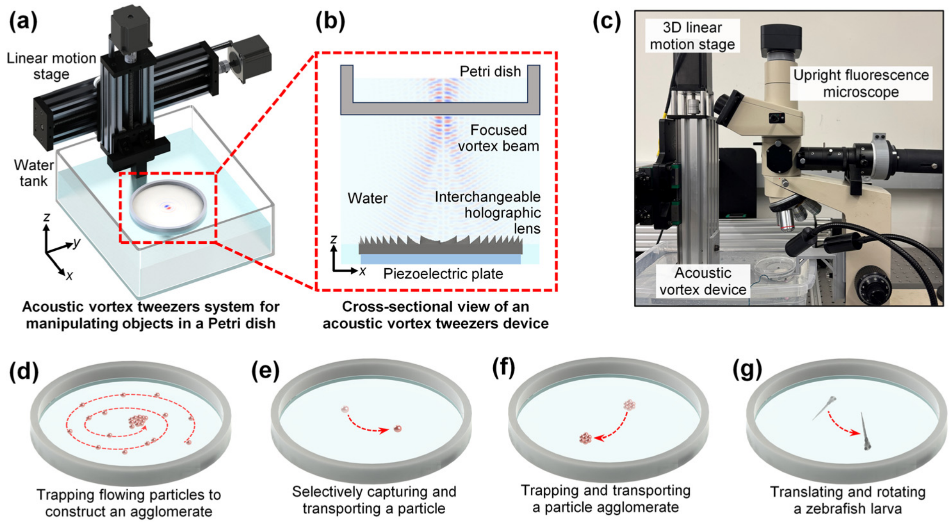

Fig. 1 Schematics and a photo of an acoustic vortex tweezers system for contactless, programmable, and multifunctional manipulation of tiny objects in Petri dishes. (a) Schematic of the in-Petri-dish acoustic vortex tweezers system, consisting of an acoustic vortex tweezers device and a 3-DoF linear motion stage. The acoustic vortex tweezers device is positioned beneath the Petri dish and connected to the 3-DoF linear motion stage. (b) A cross-sectional view for illustrating the mechanism of acoustic vortex tweezers. A focused vortex beam is generated by the holography-based acoustic device, penetrating the Petri dish's bottom wall to create an acoustic potential well for contactless manipulation of tiny objects in the Petri dish. (c) Photo of our test setup that integrates an acoustic vortex device, an upright fluorescence microscope, and a 3D linear motion stage. (d–g) Multifunctional manipulation of tiny objects enabled by our in-Petri-dish acoustic vortex tweezers system. The key functions include (d) trapping flowing particles to construct an agglomerate, (e) selectively capturing and transporting a particle, (f) trapping and transporting a cluster of particles or a particle agglomerate, and (g) trapping and translating a zebrafish larva in a Petri dish.

of the lens, and k_{lens} and k_{f} are the wavenumbers of pressure acoustic waves in the lens and surrounding fluid, respectively. Here, the lens thickness profile $h(\mathbf{x})$ is carefully designed using the approach presented in Section S1.† As shown in Fig. 2, the phase shift $\Delta\phi(\mathbf{x})$ contains two components for focusing acoustic waves and introducing an angular phase variation with a topological charge number of Q, respectively. With the designed thickness profile $h(\mathbf{x})$, an acoustic lens can be manufactured using high-resolution stereolithography 3D printing and then integrated with a circular piezoelectric transducer to construct an acoustic vortex device. Fig. 3 shows photos of 3D printed lenses and integrated acoustic devices for generating focused vortex beams with topological charge numbers of $Q = 1$, 3, and 5.

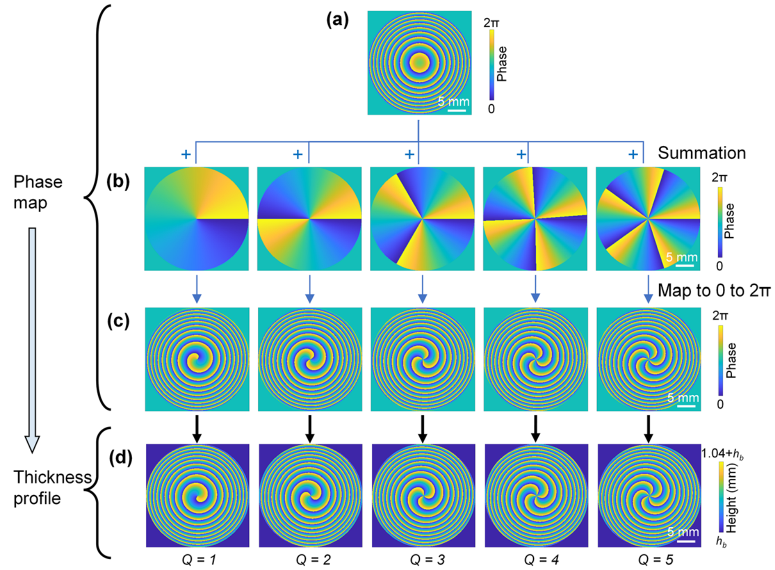

Fig. 2 Different designs of holographic acoustic lenses. (a) Phase profile determined using eqn (S1)† for generating a focused acoustic beam. (b, left to right) phase profiles for generating acoustic vortices with topological charge numbers ranging from Q =1 to 5. (c) Phase profiles for generating focused vortex beams with topological charge numbers ranging from Q =1 to 5. (d) Thickness maps of holographic lenses corresponding to the phase profiles in (c). The base thickness (h_{b}) of each lens is 1 mm.

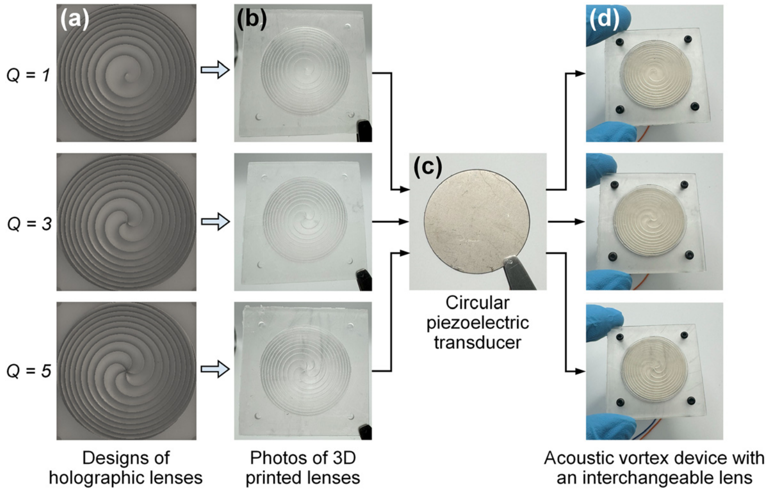

Fig. 3 Photos of focused acoustic vortex tweezers devices. (a) Designs and (b) photos of holographic lenses for generating focused vortex beams with topological charge numbers of Q = 1, 3, and 5. (c) Photo of a circular piezoelectric transducer. (d) Photos of the assembled focused acoustic vortex tweezers devices.

The interference of phase-modulated, transmitted acoustic waves, which carry the phase information $\Delta\phi(\mathbf{x})$, can generate a focused acoustic vortex beam with a topological charge number of Q. This focused vortex beam has a minimal energy core surrounded by a high-energy outer region, as illustrated by Fig. 1(b). As the acoustic energy is focused, it is strong enough to penetrate a Petri dish's bottom wall to produce an acoustic potential well in the liquid preloaded in the Petri dish, thus applying an acoustic radiation force to trap a tiny object in the liquid at the acoustic potential well's center. Moreover, the combination of the acoustic vortex device and a high-resolution, 3-DoF linear motion stage allows our integrated system to achieve automated, high-precision, versatile, and contactless manipulation of small objects in Petri dishes. The integrated acoustic vortex tweezers platform enables multiple functions, including actively concentrating particles to create a large particle cluster (illustrated in Fig. 1(d)), high-resolution transportation of a particle trapped in the vortex beam's center potential well along an arbitrary path (shown in Fig. 1(e)), trapping flowing particles using the center potential well to gradually create a particle agglomerate and then transporting the agglomerate along a customized path (see Fig. 1(f)), as well as trapping, transporting, and rotating a zebrafish larva (see Fig. 1(g)). These abilities of our acoustic vortex tweezers platform have been successfully demonstrated through a series of proof-of-concept experiments. Their results with the acoustic vortex device's characterization data are presented below.

Focused vortex beams with different topological charge numbers for generating potential wells with different sizes

To better understand the focused acoustic vortex beam-based object manipulation approach, we compared focused acoustic vortex beams with different topological charge numbers ranging from 1 to 5. Using the approach in Section S1,† we designed the thickness profiles (see Fig. 2(d)) of holographic lenses corresponding to those five cases. They are for generating 3.35 MHz focused acoustic vortex beams, which have focused energy at locations 23 mm away from their lenses, while different topological charge numbers ranging from 1 to 5. To compare their resulted focused acoustic vortex beams, we used an analytical model (see Section S2 and Fig. S1† for more details) to quickly predict their corresponding acoustic pressure and intensity fields.

Fig. 4(b, left to right) shows the simulated acoustic intensity fields in planes 23 mm away from the lenses for cases with topological charge numbers ranging from 1 to 5, and Fig. 4(c) compares their corresponding acoustic pressure fields. The intensity fields all show ring-shaped patterns with minimal intensity cores due to destructive wave interference. The ring's diameter becomes larger with the increase of the topological charge number, indicating the gradual size increase of the acoustic potential well that is for trapping tiny objects. On the other hand, the pressure fields reveal the angular phase variations depending on topological charge numbers. For example, when the topological charge number is Q = 5, the pressure field in Fig. 4(c, right) shows five peaks and five valleys alternatively presented along the angular direction. This indicates a total phase variation of $Q\cdot2\pi$.

Fig. 4(d) shows the generated acoustic intensity fields in the xz-plane. As acoustic waves emitted from an acoustic vortex device propagate away from the device, the intensity field gradually shrinks and then expands, manifesting a neck-like distribution. It can be seen that the neck region has much higher intensities than other regions. Inside the intensity neck, there is a minimal intensity core, corresponding to the center acoustic potential well observed in Fig. 4(b). It can also be seen that the minimal intensity core's width gradually increases with the increase of the topological charge number from Q = 1 to 5.

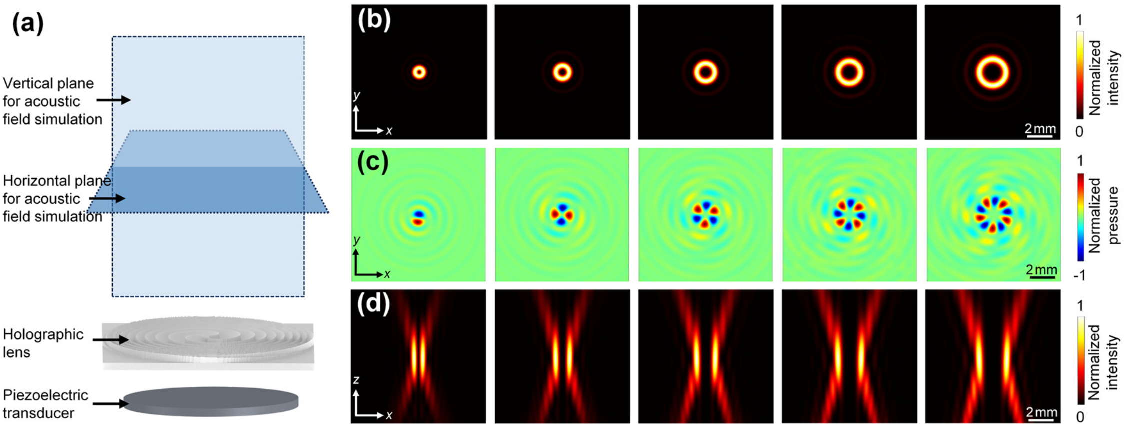

Fig. 4 Generation of focused acoustic vortex beams with different topological charge numbers using interchangeable lenses. (a) A schematic for illustrating the mechanism of generating a focused vortex beam and showing the planes for simulating acoustic fields. (b) Simulated acoustic intensity and (c) pressure fields in horizontal planes 23 mm away from holographic lenses with *Q* =1 to 5 (left to right). (d) Simulated acoustic intensity fields in the vertical planes for the five cases with *Q* = 1 to 5.

As the additively manufactured holographic lenses are interchangeable, our acoustic vortex tweezers platform can generate acoustic vortex beams with different parameters (*e.g.*, those with different topological charge numbers in Fig. 4) by simply changing the holographic lens. This allows for easily generating acoustic potential wells with desired sizes in a Petri dish, thus manipulating tiny objects ranging from micrometers to millimeters. This interchangeable design also allows for enabling more functions of manipulating tiny objects, such as trapping and manipulating micrometer-scaled particles and cells, manipulating millimeter-scaled zebrafish larvae, as well as concentrating tiny particles to construct a particle agglomerate with a controlled diameter.

Concentrating tiny objects by shrinking an acoustic potential well

No studies have investigated the effect of a gradually shrinking acoustic potential well on the distribution of in-liquid micro-objects. As the focused acoustic vortex beam has a gradually shrinking and then expanding intensity profile, as revealed by acoustic fields in Fig. 4(d), it becomes possible to gradually adjust the size of a potential well in a fixed plane (for example, a plane at the bottom of a position-fixed Petri dish), by gradually adjusting the distance from the holographic lens to the Petri dish's bottom wall. This feature allows for generating different-sized potential wells with a single focused acoustic vortex beam, only by adjusting the distance, thus enabling unique object manipulation strategies. In practice, the distance adjustment can precisely be achieved by controlling the z-translation of our high-resolution 3D linear motion stage, where the acoustic vortex device is installed.

To demonstrate the ability to change the size of a ring-shaped acoustic potential well, a series of acoustic field characterization experiments were performed. We acquired the acoustic fields generated in horizontal planes having different distances to the holographic lens, ranging from Δz = 19 to 23 mm. The experimentally acquired pressure and intensity fields in Fig. 5(a) and (c) are consistent with the analytical simulation results in Fig. 5(b) and (d). They both show that the generated acoustic potential well's diameter gradually reduces, as the distance from the fixed target plane to the acoustic device gradually increases from 19 to 23 mm. The ring-shaped potential well results in a trapping force (*i.e.*, acoustic radiation force's radial component) toward the well's center, as shown in Fig. 5(e), critical for trapping micro-objects. With the increase of distance Δz from 19 to 23 mm, the maximum trapping force gradually increases from 94 to 953 pN.

Additionally, to better understand the effect of acoustic reflection at the air–liquid interface on the generated vortex beam, we performed finite element simulations for cases with and without the interface reflection. As shown by the simulated acoustic field in Fig. 6(a–c), after the forward acoustic waves pass through the focal plane, the waves begin to diverge. When the waves obliquely impinge on the air–liquid interface, the reflected waves propagate in directions away from the vortex beam's center. Consequently, the acoustic waves reflected from the air–liquid interface have negligible effects on the generated acoustic trap at the bottom of the Petri dish, as revealed by the comparison between cases with (Fig. 6(c)) and without (Fig. 6(d)) reflected waves from the air–liquid interface. Additionally, a relatively thick liquid layer in the Petri dish is preferred, as a thicker liquid layer leads to more diverged waves reflected from the air–liquid interface, as shown by the comparison among simulation results for cases with 1 mm, 2 mm, and 3 mm thick liquid layers in Fig. 6(a–c).

By adjusting the distance Δz between the acoustic device and the object manipulation plane using the 3D linear motion stage, our integrated acoustic vortex tweezers system can tune an acoustic potential well's size

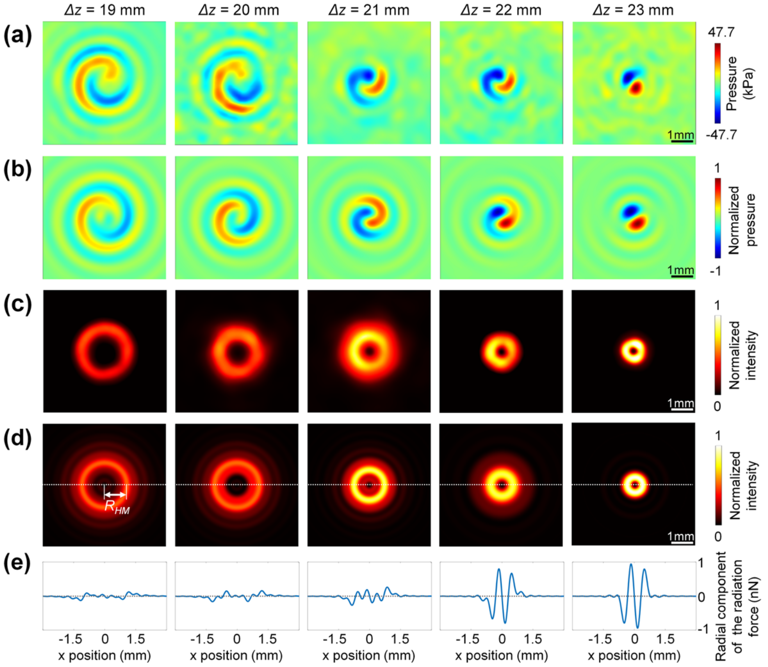

Fig. 5 Experimental and simulated acoustic vortex fields in horizontal planes with different distances to a Q = 1 holographic lens. (a and b) Experimental and simulated acoustic pressure fields. (c and d) Experimental and simulated acoustic intensity fields. (e) Simulated acoustic radiation force (radial component) applied on a 75 μm polystyrene particle on a line passing the vortex center (illustrated in d). The input acoustic pressure value for this simulation is set to the experimentally measured pressure. The first to fifth columns are for cases with distances of Δz = 19, 20, 21, 22, and 23 mm, respectively. For pressure field measurement, the input power applied to the piezoelectric transducer at the operation frequency of 3.35 MHz was set to 1.27 W.

on-demand for manipulating objects preloaded in a position-fixed Petri dish. With the setup illustrated in Fig. 7(a), a validation experiment was performed by concentrating microparticles in a Petri dish. The acquired time-sequential images in Fig. 7(b) and Movie S1† show that numerous microparticles were gradually moved to the focused acoustic vortex beam's center with the reduction of the potential well size, achieved by gradually increasing the distance from the acoustic device to the Petri dish. This experiment validates a unique particle concentration approach that hasn't been reported to the best of our knowledge.

Translating a micro-object enabled by a micrometer-scaled potential well of a focused vortex beam with Q = 1

To selectively trap an object using an acoustic potential well, it is preferred that the acoustic potential well has a

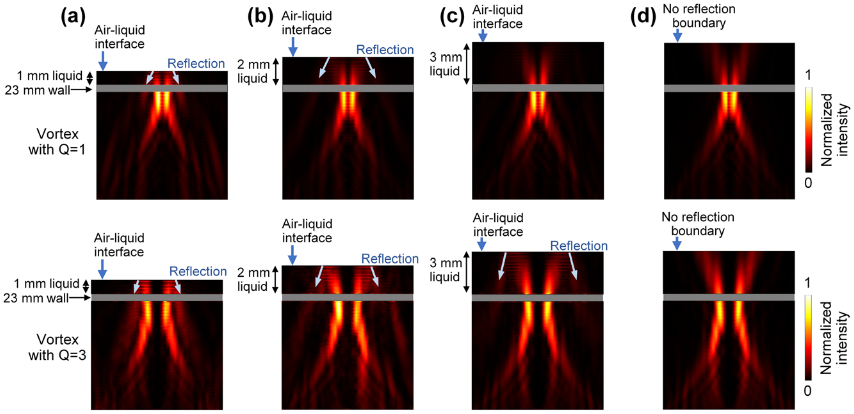

Fig. 6 Simulated acoustic wavefields to understand the effect of wave reflection at the air–liquid interface on a focused vortex beam. (a–c) Simulated intensity fields when a Petri dish contains 1 mm, 2 mm, and 3 mm thick water layers, respectively. (d) Simulated intensity field when not considering the boundary reflection. The top and bottom rows correspond to focused vortex beams with topological charge numbers of 1 and 3, respectively.

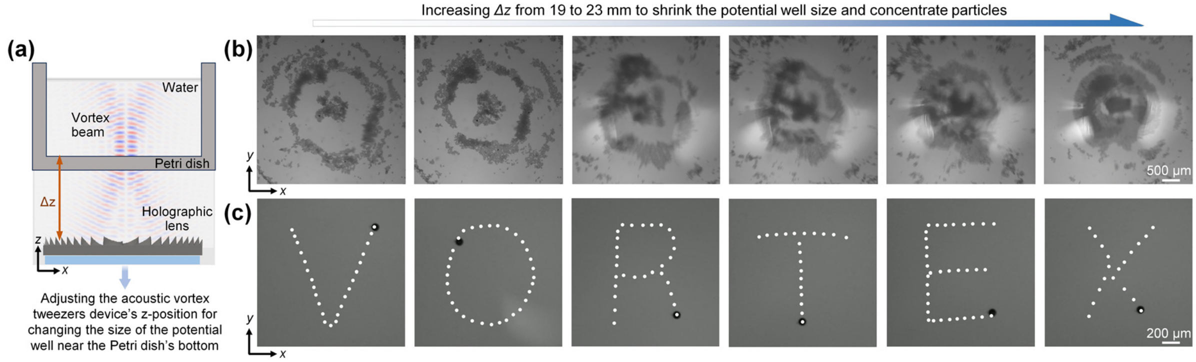

Fig. 7 In-Petri-dish particle concentration and single-particle translation enabled by acoustic vortex tweezers with a topological charge number of $Q = 1$. (a) A schematic of the test setup. (b) Sequential images showing the particle concentration process when decreasing the distance Δz and shrinking the potential well size. (c) Translation of a 75 μm diameter polystyrene particle in a Petri dish to write the letters ‘VORTEX’.

diameter comparable to the object's size. When the topological charge number Q equals 1, the acoustic potential well of the focused vortex beam generated by our device at 3.35 MHz has a very small diameter in its focal plane. By measuring the distance R_{HM} (illustrated in Fig. 5(d), left) from the potential well's center to an inner half-maximum-intensity point of the generated acoustic intensity ring in the focal plane, we found that the minimal potential well diameter defined by $2R_{\mathrm{HM}}$ was approximately 310 μm. Such micrometer-scale potential well allows our system to trap and manipulate a single micro-object. To demonstrate this ability, we performed proof-of-concept experiments, by using the $Q = 1$ focused acoustic vortex beam to selectively capture a 75 μm diameter polystyrene particle in a solution with numerous particles preloaded into a Petri dish. By further controlling the 3D linear motion stage where the acoustic vortex device was installed, the acoustically trapped single particle was translated along desired paths in a precise and programmable manner. The captured microscopic images in Fig. 7(c) and the recorded Movie S2† show that a 75 μm polystyrene particle in a Petri dish was successfully trapped by the $Q = 1$ focused vortex beam and transported along complex trajectories to write high-resolution letters ‘VORTEX’.

Capturing flowing micro-objects to create an agglomerate and translating the agglomerate using a focused vortex beam with $Q = 3$

Our acoustic vortex tweezers system is able to capture flowing micro-objects to create a large agglomerate and translate the agglomerate along complex paths. To demonstrate this ability, we used an experimental setup illustrated in Fig. 8(a). The acoustic device placed beneath a Petri dish is customized to generate a focused vortex beam with a topological charge number of $Q = 3$, as this beam's potential well is large enough (with a diameter $2R_{\mathrm{HM}} \approx 1150$ μm) to capture numerous micro-objects for creating an agglomerate. Moreover, the large acoustic potential well ensures the continuous trapping and protection of the agglomerate, thus allowing our integrated system to translate the agglomerate.

The time-sequential images in Fig. 8(b) and Movie S3† reveal the formation process of gradually creating the large particle cluster, by trapping flowing microparticles using a focused acoustic beam with $Q = 3$. It can be seen that the particle cluster's diameter gradually increases to ~0.9 mm in 108 s. Moreover, leveraging our integrated acoustic vortex tweezers system, we can transport the formed particle cluster in the Petri dish in a programmable and contactless manner. The sequential images in Fig. 8(c) and Movie S4†

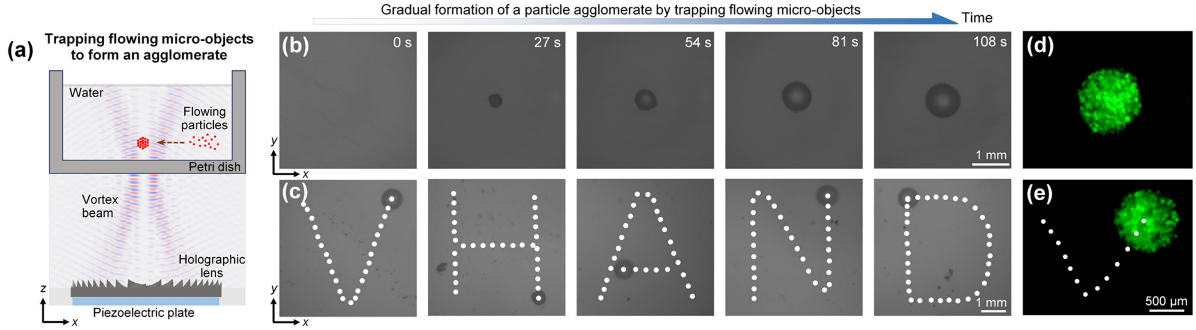

Fig. 8 Trapping flowing particles and transporting a cluster of particles enabled by acoustic vortex tweezers with a topological charge number of $Q = 3$. (a) A schematic illustrating the trapping of flowing particles using in-Petri-dish acoustic vortex tweezers. (b) Sequential images showing the trapping of flowing particles to construct a particle cluster whose diameter gradually increased to 0.9 mm. (c) In-Petri-dish translation of the formed particle cluster to write the letters ‘VHAND’. (d and e) Results demonstrating the construction and translation of a cell cluster, respectively.

demonstrate the transportation of a particle cluster along pre-defined trajectories to spell 'VHAND' in the Petri dish. In addition to manipulating microparticles, we demonstrated the ability to concentrate cells as shown in Fig. 8(d) and Movie S5,† as well as transport a cell cluster along a desired trajectory as shown in Fig. 8(e) and Movie S6.†

Multi-DOF manipulation of zebrafish larvae using a millimeter-scaled potential well of a focused vortex beam with *Q* = 5

Zebrafish, a model organism for biological and biomedical research, plays a critical role in studying vertebrate developmental biology and human genetic diseases.[67] Platforms capable of handling, translating, and rotating small zebrafish larvae without direct contact and in a programmed manner are highly desired, as they hold great potential for transporting zebrafish larvae, sorting them into different categories, as well as rotating them to capture images from different directions for reconstructing zebrafish 3D profiles, thereby facilitating biological and biomedical research.

As the holographic lens of our acoustic vortex tweezers system is interchangeable, it can be easily changed for generating a focused vortex beam with a topological charge number of $Q = 5$. This results in a millimeter-scaled acoustic potential well more suitable for trapping zebrafish larvae, compared to micrometer-scaled vortex potential wells with smaller topological charge numbers. By leveraging a focused vortex beam with $Q = 5$, our integrated acoustic vortex tweezers system allows for multi-DoF translational and rotational manipulation of zebrafish larvae in Petri dishes. We performed a series of proof-of-concept experiments, wherein our system was used to manipulate a zebrafish larva (fixed 5-day post-fertilization) preloaded into the Petri dish in an automated, contactless, and programmable manner. Particularly, we demonstrated that a zebrafish larva could be horizontally and vertically trapped in a Petri dish and then rotated and translated without direct contact. Such multi-DoF, contactless, in-Petri-dish

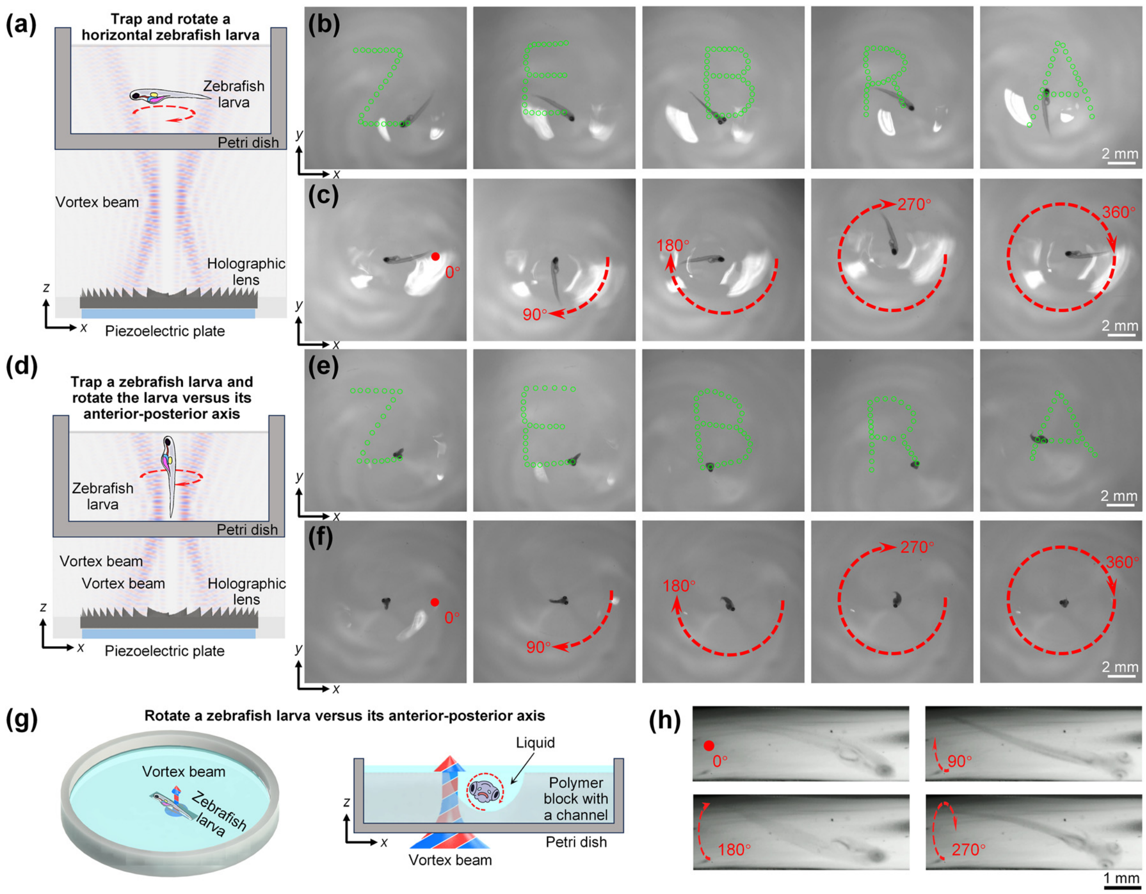

Fig. 9 Trapping, rotating, and transporting single zebrafish larvae in a Petri dish enabled by acoustic vortex tweezers with a topological charge number of $Q = 5$. (a) Schematic illustrating the manipulation of a horizontal zebrafish larva in a Petri dish. (b) Transporting a horizontally trapped zebrafish larva in a Petri dish to write the letters 'ZEBRA'. (c) Clockwise rotation of a horizontally trapped zebrafish larva. (d) Schematic illustrating the manipulation of a vertical zebrafish larva in a Petri dish. (e) Transporting a vertically trapped zebrafish larva in a Petri dish to write the letters 'ZEBRA'. (f) Clockwise rotation of a vertically trapped zebrafish larva with respective to its anterior–posterior axis. (g) 3D and 2D schematics illustrating the manipulation of a horizontal zebrafish larva using an asymmetric acoustic field. (h) Images acquired from different angles of a zebrafish when it was rotated with respect to its anterior–posterior axis.

manipulation capability has not been demonstrated to the best of our knowledge.

Fig. 9(a) illustrates our experimental setup for trapping a zebrafish larva in a horizontal posture in a Petri dish and then translating and rotating the larva. To achieve this manipulation ability, we first adjusted the distance between the Petri dish and the acoustic device. This allowed us to control the size of a cone-like acoustic potential field inside the Petri dish so that the cone size was large enough to effectively trap a zebrafish larva in a horizontal posture. Once trapped, the larva could be translated using the 3-DoF linear motion stage. The acquired time-sequential images in Fig. 9(b) and Movie S7† show the successful trapping of a zebrafish larva in a horizontal posture, as well as the automated translation of the zebrafish along complex paths, writing the word 'ZEBRA'. In addition to trapping and translation, the acoustic vortex beam's angular momentum can rotate the trapped zebrafish larva. The acquired time-sequential images in Fig. 9(c) and Movie S9† show the clockwise rotation of a horizontally trapped zebrafish larva with respect to its dorsal-ventral axis, consistent with the vortex beam's angular momentum direction. For these experiments, the zebrafish larva was fixed on the fifth day post fertilization. In the future, we will conduct experiments with live zebrafish larvae and investigate the acoustic effect of their viability.

Fig. 9(d) shows the experimental setup for in-Petri-dish trapping of a zebrafish larva in a vertical posture and then translating and rotating the vertical larva. By adjusting the distance between the Petri dish and the acoustic device, our system can narrow down the size of the cone-like acoustic intensity field generated in the Petri dish. This narrow energy cone allows for trapping a zebrafish larva in a vertical posture. Moreover, our acoustic vortex tweezers system can precisely and robustly translate the trapped larva along customized trajectories, for example, trajectories to write the word 'ZEBRA' as validated by our experimental results in Fig. 9(e) and Movie S8.† Additionally, owing to the angular momentum applied by the focused vortex beam, the vertically trapped zebrafish can be rotated in the same clockwise direction with respect to the anterior–posterior axis, as proven by the acquired time-sequential images in Fig. 9(f) and Movie S9.† Although this experiment demonstrates the ability to rotate a zebrafish with respect to its anterior–posterior axis, images captured by a camera above the dish are not suitable for 3D reconstruction of the zebrafish. To address this issue, one possible solution is to add a camera to capture images from the lateral side of the zebrafish, which will be tested in our future studies. Another approach, which does not require a side camera, involves using an asymmetric acoustic field. As illustrated in Fig. 9(g), a polymer block with a 2 mm-wide channel, open at the top, was placed in a Petri dish. The vortex beam's axis was aligned with the channel side wall, thereby generating an acoustic field asymmetric to the channel centerline. Because of this asymmetric field, a zebrafish larva was successfully rotated with respect to its anterior–posterior axis, allowing images to be captured from different angles (see Fig. 9(h) and Movie S10†).

Conclusion and discussion

This study presents an in-Petri-dish acoustic vortex tweezers system, which integrates an acoustic holography-based vortex tweezers device and a 3-DoF high-resolution linear motion stage, for enabling contactless, multi-DoF, multifunctional, programmable, and high-resolution manipulation of small objects (ranging from micrometers to millimeters) within a Petri dish. The acoustic vortex tweezers device comprises a holographic acoustic lens that transforms incident acoustic waves generated by a circular piezoelectric transducer into a focused acoustic vortex beam, which carries sufficient energy to transmit through a Petri dish's bottom wall and create a ring-shaped acoustic intensity field inside the Petri dish, allowing for the trapping and manipulation of tiny objects. By encoding phase profiles with different topological charge numbers into the thickness profile of the holographic lens, our acoustic vortex device can generate different-sized ring-shaped acoustic intensity fields near a Petri dish's bottom, thereby accommodating the trapping of different-sized objects. Moreover, the acoustic vortex device can apply torque to a trapped object, enabling its rotational manipulation. Additionally, integrating our acoustic vortex tweezers with a customized 3-DoF linear motion stage offers a variety of manipulation strategies, including tuning potential well sizes by controlling the z-position of the acoustic device and programmable translation of acoustically trapped objects along complex paths. It is also worth noting that our approach potentially works for various Petri dishes and well-plates, as our experiments showed that the generated acoustic vortex beams can transmit through 0.9 mm glass and 2.6 mm acrylic plates to trap microparticles (see Fig. S2†).

To demonstrate the versatile capabilities of our in-Petri-dish acoustic vortex tweezers system, we conducted a series of proof-of-concept experiments. First, we demonstrated a unique approach based on the gradual shrinking of an acoustic potential well for concentrating microparticles dispersed in a Petri dish. By adjusting the distance between the acoustic vortex device and the Petri dish, we gradually decreased the size of the acoustic potential well in the Petri dish, thereby concentrating microparticles within it. Second, using holographic lenses encoded with different topological charge numbers, we generated ring-shaped acoustic intensity fields with different diameters, enabling the trapping and translation of different-sized objects, such as microparticles, cells, and zebrafish larvae. Together with a 3-DoF linear motion stage, our integrated system was demonstrated by translating trapped objects along desired trajectories, such as complex high-resolution paths depicting different letters. Third, we showed that flowing microparticles in a Petri dish could be trapped and gradually aggregated, allowing for the creation of a particle cluster with a desired diameter, which could then be translated along complex paths. Fourth, we demonstrated multi-DoF, multifunctional manipulation of a zebrafish larva in a Petri dish, including trapping the larva in horizontal and vertical postures, translating it along complex paths, as well as rotating it with respect to its dorsal-ventral and anterior–posterior axes.

Compared to previous acoustic vortex-based contactless object manipulation methods,[8,9,61,62] our approach enables the manipulation of small objects in commercial Petri dishes, thereby minimizing cross-contamination, eliminating the need for customized microfluidic chambers/channels, and making it suitable for integration into laboratory workflows. Second, our approach considers the minimization of the influence of acoustic waves reflected by the air–liquid interface, which was not considered in previous methods. Third, our approach allows for gradual adjustment of the acoustic potential well size by controlling the distance between the acoustic device and the object manipulation plane. By this means, the acoustic tweezers can be adapted for objects of different sizes. Small objects distributed over a large region can be gradually transported for concentration by gradually reducing the size of the potential well. Fourth, our approach achieves the trapping, rotation, and translation of zebrafish larvae. In addition, compared to previous acoustic vortex devices that relied on transducers with customized electrodes[61,62] and lenses with four different heights,[9] our approach with interchangeable holographic lenses allows for generating various focused acoustic vortex beams with desired charge numbers and focal lengths. Compared to previous works on acoustics-based contactless manipulation of objects in Petri dishes and multi-well plates,[43,44] the approach presented in this paper offers more functionalities, such as transporting different-sized objects (*e.g.*, single micro-objects, cell/particle clusters, and zebrafish larvae) along customized paths and rotating the trapped objects.

In our future work, we will address multiple limitations of this study and continue to improve this vortex beam-based technology. First, this study mainly focuses on the effect of acoustic radiation force with the acoustic streaming effect not explored. To fill this gap, we will explore the acoustic vortex beam-based control of acoustic streaming and the manipulation of objects smaller than the cells and microparticles used in this study. As the object size decreases, the acoustic streaming-induced drag force plays an increasingly important role in influencing the object's motion. As shown by our simulation results in Fig. S3,† the vortex acoustic beam induces vortex streaming that flows toward the vortex center. In the future, we will test the ability of this vortex streaming to trap and manipulate submicron objects. Second, when continuously generating acoustic waves, we observed oscillations at the liquid–air interface, which caused distortions in the acquired images. To address this limitation, we will test and optimize a cyclic on–off operation mode with acoustic waves on for object manipulation and off for image acquisition. Third, in our current experimental setup (see Fig. 1(c)), the bottom part of an upright microscope was removed for the installation of acoustic devices. We will continue to upgrade the vortex beam technology to enhance its compatibility with both inverted and upright microscopes. In the long run, we expect to achieve a cost-effective and easy-to-use tool that researchers in the biomedical and biological communities can use for the programmable and contactless handling of objects ranging from micrometers to millimeters, thereby facilitating biomedical and biological research.

Materials and methods

Design, fabrication, and operation of acoustic vortex devices

The focused acoustic vortex tweezers devices utilized in this work are composed of an interchangeable holographic lens and a circular piezoelectric plate transducer, coupled through a thin (~0.2 mm thick) layer of ultrasound couplant in between. The method for determining the holographic lens thickness profile is given in Section S1.† The lens was fabricated using a photocurable resin (RS-F2-GPCL-04, Formlabs) and a stereolithography 3D printer (form 3, Formlabs) with an *XY* resolution of 25 μm and a minimum printing thickness of 25 μm. These parameters are much smaller than the wavelength of acoustic waves at the device frequency of 3.35 MHz. Each fabricated lens has a thickness profile varying from h_b to h_b + 1.04 mm, where h_b = 1 mm is the base thickness. This variation allows for introducing phase differences covering the 0 to 2π range in the transmitted waves. The circular piezoelectric transducer (SMD28T07F3000R, Steiner & Martins Inc.) made of lead zirconate titanate (PZT) has a diameter of 28 mm and a thickness of 0.7 mm. It has a thickness-mode resonant frequency of 3.35 MHz confirmed by a laser Doppler vibrometer. As shown by the photos in Fig. 3, multiple holographic lenses were fabricated, and they can be interchanged to generate acoustic vortex beams with desired topological charge numbers such as Q = 1, 3, and 5.

To generate a focused vortex beam using our device, a sinusoidal signal at 3.35 MHz is generated by a function generator (DG1022Z, RIGOL) and then amplified by a power amplifier (A075, Electronics & Innovation Ltd.). For 3.35 MHz acoustic waves transmitting through the bottom wall (material: polystyrene, thickness: 1.1 mm) of the Petri dish, the power transmission coefficient is ~62.33%. In practice, the energy loss associated with transmission reduction can be addressed by increasing the input power to the piezoelectric transducer. We found that an input power of 0.26 W was sufficient to manipulate microparticles and cells using our acoustic vortex device.

Analytical simulations

We used an analytical model to predict the acoustic pressure and intensity fields generated by our holography-based acoustic devices. The details of the analytical model can be found in Section S2 and Fig. S1.† With this model, we obtained the acoustic pressure and intensity fields in Fig. 4 for acoustic vortex devices with different holographic lenses at the same excitation frequency of 3.35 MHz. We also obtained the pressure and intensity fields in Fig. 5 for planes with different distances to the acoustic device.

Translation of an acoustically trapped object

To achieve programmable translation of an acoustically trapped object in a Petri dish, we integrated our acoustic device for generating a focused vortex beam with a customized 3-DoF linear motion stage. A motion controller (Openbuilds) with a micro-stepping motor control function was used to control all the step motors of the customized 3-DoF linear motion stage for precise translational motions in *x*-, *y*-, and *z*-directions with a resolution of 6.25 μm. The motion controller was connected to a computer through serial communication, for enabling programmable translation of the acoustically trapped object along customized paths.

To manipulate microscale objects, our acoustic device was placed under an upright fluorescence microscope (Olympus BH-2) equipped with 2.5X, 10X, and 20X objectives, as shown in the setup in Fig. 1c. After adding particles or cells with densities greater than that of the medium, they sedimented to the bottom of the Petri dish due to gravity. Acoustic waves were then activated for contactless manipulation. A camera (ToupCam) installed on the microscope was used to capture time-sequential images and record videos. Although our approach can translate microscale objects in the *xy*-plane, it still lacks the ability to precisely move trapped objects in the *z*-direction.

Reagents and materials

To demonstrate the ability to manipulate micro-objects, we used 75 μm polystyrene particles (BKPMS, Cospheric) in deionized water. Zebrafish larvae (*nacre* hetrozygous) used for this study were raised at 28.5 °C under normal light/dark cycle, as described previously.[68] The larvae were fixed on the fifth day post fertilization in 4% paraformadehype and stored in PBS at 4 °C. For acoustic manipulation experiments, each larva was loaded into a Petri dish with deionized water. All zebrafish experiments were conducted with approval from the Virginia Tech Animal Care and Use Committee. All experiments were performed in compliance with the relevant institutional guidelines of Virginia Tech.

Cell culture and staining

The human glioblastoma cell line, U251 cells were used to demonstrate cell cluster formation and manipulation in this study. The U251 cells were cultured in Dulbecco's Modified Eagle's Medium (DMEM, GenClone, USA) supplemented with high glucose and L-glutamine, 10% fetal bovine serum (Gibco, Life Technologies), penicillin (50 units mL^{-1}, Sigma-Aldrich), and streptomycin (50 μg mL^{-1}, Sigma-Aldrich), maintained in a 37 °C, 5% carbon dioxide (CO_2) incubator. Prior to the experiment, U251cells were resuspended in fresh phosphate-buffered saline (PBS, pH ~7.4) to achieve a concentration of approximately 1.0×10^6 cells per mL.

Acoustic field characterization

To characterize the generated acoustic pressure and intensity fields, we used a hydrophone (HNR-0500, ONDA Co.) mounted on a customized 3D linear motion stage (see Fig. S4†). The hydrophone was connected to an oscilloscope (SDS 1202-E, SIGLENT) that was to record the time-domain waveforms. A function generator (DG1022Z, RIGOL) was employed to provide the excitation signal for the acoustic device. The diagram in Fig. S5† summarizes key steps to acquire acoustic pressure and intensity fields. By changing the hydrophone position in a point-by-point manner and acquiring acoustic pressure waveforms at a series of points on a grid in the desired wavefield characterization region, we can obtain a series of time-domain waveforms registered at all the scanning points. At each point, we captured 8 waveforms and then averaged them to increase the signal-to-noise ratio. The fusion of waveforms acquired at all the scanning points leads to a time–space wavefield $S_{\text{ts}}(t, \mathbf{x})$ containing the wave propagation information. By applying the Fourier transform to the time–space wavefield, a frequency-space wavefield $S_{\text{fs}}(f, \mathbf{x})$ can be acquired, for further obtaining the intensity field $|S_{\text{fs}}(f_{\text{i}}, \mathbf{x})|^2$ at a selected frequency of f_{i}.

Data availability

The data supporting this article have been included as part of ESI.†

Author contributions

T. L. and Z. T. conceived the idea. T. L. and J. L. designed and manufactured the focused acoustic vortex device. T. L., C. Q., and Z. W. performed acoustic field characterization experiments. T. L. and B. C. performed contactless particle manipulation experiments. T. L. and L. B. performed analytical simulations. M. R. B., Y. D., and Y. A. P. prepared the biological samples. All the authors contributed to the paper writing. Z. T. supervised the study.

Conflicts of interest

There are no conflicts to declare in this manuscript.

Acknowledgements

The authors acknowledge the financial support from the National Institute of General Medical Sciences of the National Institute of Health (7R01GM144417), the National Science Foundation (CMMI 2243771 and CMMI 2340016), and the Nuclear Energy University Program (DE-NE0009187).

References

1 D. G. Grier, *Nature*, 2003, **424**, 810–816.

2 A. Ashkin, J. M. Dziedzic and T. Yamane, *Nature*, 1987, **330**, 769–771.

3 J. Voldman, *Biomed. Eng.*, 2006, **8**, 425–454.

4 M. Krishnan, N. Mojarad, P. Kukura and V. Sandoghdar, *Nature*, 2010, **467**, 692–695.

5 I. D. Vlaminck and C. Dekker, *Biophysics*, 2012, **41**, 453–472.

6 S. H. Leuba, M. A. Karymov, M. Tomschik, R. Ramjit, P. Smith and J. Zlatanova, *Proc. Natl. Acad. Sci. U. S. A.*, 2003, **100**, 495–500.

7 J. Wu, *J. Acoust. Soc. Am.*, 1991, **89**, 2140–2143.

8 T. Li, J. Li, L. Bo, H. Bachman, B. Fan, J. Cheng and Z. Tian, *Sci. Adv.*, 2024, **10**, eadm7698.

9 J. Heo, W. Choi, J. Key, I. Youn and S. Han, *Int. J. Mech. Sci.*, 2023, **260**, 108635.

10 D. Foresti, M. Nabavi, M. Klingauf, A. Ferrari and D. Poulikakos, *Proc. Natl. Acad. Sci. U. S. A.*, 2013, **110**, 12549–12554.

11 A. Marzo, S. A. Seah, B. W. Drinkwater, D. R. Sahoo, B. Long and S. Subramanian, *Nat. Commun.*, 2015, **6**, 8661.

12 K. Melde, A. G. Mark, T. Qiu and P. Fischer, *Nature*, 2016, **537**, 518–522.

13 K. Melde, E. Choi, Z. Wu, S. Palagi, T. Qiu and P. Fischer, *Adv. Mater.*, 2018, **30**(3), 1704507.

14 H. G. Lim and K. K. Shung, *Ann. Biomed. Eng.*, 2017, **45**, 2174–2183.

15 J. Dual and T. Schwarz, *Lab Chip*, 2011, **12**, 244–252.

16 D. Carugo, T. Octon, W. Messaoudi, A. L. Fisher, M. Carboni, N. R. Harris, M. Hill and P. Glynne-Jones, *Lab Chip*, 2014, **14**, 3830–3842.

17 A. Marzo, M. Caleap and B. W. Drinkwater, *Phys. Rev. Lett.*, 2018, **120**, 044301.

18 Y. Yang, Y. Yang, D. Liu, Y. Wang, M. Lu, Q. Zhang, J. Huang, Y. Li, T. Ma, F. Yan and H. Zheng, *Nat. Commun.*, 2023, **14**, 3297.

19 J. Friend and L. Y. Yeo, *Rev. Mod. Phys.*, 2011, **83**, 647–704.

20 Y. Q. Fu, J. K. Luo, N. T. Nguyen, A. J. Walton, A. J. Flewitt, X. T. Zu, Y. Li, G. McHale, A. Matthews, E. Iborra, H. Du and W. I. Milne, *Prog. Mater. Sci.*, 2017, **89**, 31–91.

21 B. W. Drinkwater, *Lab Chip*, 2016, **16**, 2360–2375.

22 P. Dumčius, R. Mikhaylov, X. Zhang, M. Bareford, M. Stringer, R. Errington, C. Sun, E. Gonzalez, T. Krukovski, J. M. Falcon-Perez, D. Liang, Y. Fu, A. Clayton and X. Yang, *Small*, 2023, **19**, e2300390.

23 B. Sridharan and H. G. Lim, *Mater. Today Bio*, 2023, **19**, 100556.

24 M. Wu, Y. Ouyang, Z. Wang, R. Zhang, P.-H. Huang, C. Chen, H. Li, P. Li, D. Quinn, M. Dao, S. Suresh, Y. Sadovsky and T. J. Huang, *Proc. Natl. Acad. Sci. U. S. A.*, 2017, **114**, 10584–10589.

25 M. Rezeli, O. Gidlöf, M. Evander, P. Bryl-Górecka, R. Sathanoori, P. Gilje, K. Pawłowski, P. Horvatovich, D. Erlinge, G. Marko-Varga and T. Laurell, *Anal. Chem.*, 2016, **88**, 8577–8586.

26 F. Guo, P. Li, J. B. French, Z. Mao, H. Zhao, S. Li, N. Nama, J. R. Fick, S. J. Benkovic and T. J. Huang, *Proc. Natl. Acad. Sci. U. S. A.*, 2015, **112**, 43–48.

27 J. P. Lata, F. Guo, J. Guo, P. Huang, J. Yang and T. J. Huang, *Adv. Mater.*, 2016, **28**, 8632–8638.

28 S. M. Naseer, A. Manbachi, M. Samandari, P. Walch, Y. Gao, Y. S. Zhang, F. Davoudi, W. Wang, K. Abrinia, J. M. Cooper, A. Khademhosseini and S. R. Shin, *Biofabrication*, 2017, **9**, 015020.

29 B. Kang, J. Shin, H.-J. Park, C. Rhyou, D. Kang, S.-J. Lee, Y. Yoon, S.-W. Cho and H. Lee, *Nat. Commun.*, 2018, **9**, 5402.

30 C. Bouyer, P. Chen, S. Güven, T. T. Demirtaş, T. J. F. Nieland, F. Padilla and U. Demirci, *Adv. Mater.*, 2016, **28**, 161–167.

31 J. P. K. Armstrong, J. L. Puetzer, A. Serio, A. G. Guex, M. Kapnisi, A. Breant, Y. Zong, V. Assal, S. C. Skaalure, O. King, T. Murty, C. Meinert, A. C. Franklin, P. G. Bassindale, M. K. Nichols, C. M. Terracciano, D. W. Hutmacher, B. W. Drinkwater, T. J. Klein, A. W. Perriman and M. M. Stevens, *Adv. Mater.*, 2018, **30**, 1802649.

32 D. Ahmed, A. Ozcelik, N. Bojanala, N. Nama, A. Upadhyay, Y. Chen, W. Hanna-Rose and T. J. Huang, *Nat. Commun.*, 2016, **7**, 11085.

33 T. Li, J. Li, L. Bo, M. R. Brooks, Y. Du, B. Cai, Z. Pei, L. Shen, C. Sun, J. Cheng, Y. A. Pan and Z. Tian, *Adv. Mater. Technol.*, 2024, **9**(18), 2400564.

34 V. M. Jooss, J. S. Bolten, J. Huwyler and D. Ahmed, *Sci. Adv.*, 2022, **8**, eabm2785.

35 C. Chen, Y. Gu, J. Philippe, P. Zhang, H. Bachman, J. Zhang, J. Mai, J. Rufo, J. F. Rawls, E. E. Davis, N. Katsanis and T. J. Huang, *Nat. Commun.*, 2021, **12**, 1118.

36 A. D. C. Fonseca, C. Glück, J. Droux, Y. Ferry, C. Frei, S. Wegener, B. Weber, M. E. Amki and D. Ahmed, *Nat. Commun.*, 2023, **14**, 5889.

37 Y. Deng, A. Paskert, Z. Zhang, R. Wittkowski and D. Ahmed, *Sci. Adv.*, 2023, **9**, eadh5260.

38 S. Sabrina, M. Tasinkevych, S. Ahmed, A. M. Brooks, M. O. de la Cruz, T. E. Mallouk and K. J. M. Bishop, *ACS Nano*, 2018, **12**, 2939–2947.

39 D. Ahmed, M. Lu, A. Nourhani, P. E. Lammert, Z. Stratton, H. S. Muddana, V. H. Crespi and T. J. Huang, *Sci. Rep.*, 2015, **5**, 9744.

40 M. A. Ghanem, A. D. Maxwell, Y.-N. Wang, B. W. Cunitz, V. A. Khokhlova, O. A. Sapozhnikov and M. R. Bailey, *Proc. Natl. Acad. Sci. U. S. A.*, 2020, **117**, 16848–16855.

41 Y. Yang, T. Ma, S. Li, Q. Zhang, J. Huang, Y. Liu, J. Zhuang, Y. Li, X. Du, L. Niu, Y. Xiao, C. Wang, F. Cai and H. Zheng, *Research*, 2021, **2021**, 1–13.

42 W.-C. Lo, C.-H. Fan, Y.-J. Ho, C.-W. Lin and C.-K. Yeh, *Proc. Natl. Acad. Sci. U. S. A.*, 2021, **118**, e2023188118.

43 Y. Kurashina, K. Takemura and J. Friend, *Lab Chip*, 2017, **17**, 876–886.

44 P. Liu, Z. Tian, N. Hao, H. Bachman, P. Zhang, J. Hu and T. J. Huang, *Lab Chip*, 2020, **20**, 3399–3409.

45 C. Cengiz and S. Shahab, *J. Phys. D: Appl. Phys.*, 2024, **57**, 365501.

46 Y. Gu, C. Chen, Z. Wang, P.-H. Huang, H. Fu, L. Wang, M. Wu, Y. Chen, T. Gao, J. Gong, J. Kwun, G. M. Arepally and T. J. Huang, *Lab Chip*, 2019, **19**, 394–402.

47 F. Petersson, L. Åberg, A.-M. Swärd-Nilsson and T. Laurell, *Anal. Chem.*, 2007, **79**, 5117–5123.

48 S. Oberti, A. Neild and J. Dual, *J. Acoust. Soc. Am.*, 2007, **121**, 778–785.

49 D. J. Collins, C. Devendran, Z. Ma, J. W. Ng, A. Neild and Y. Ai, *Sci. Adv.*, 2016, **2**, e1600089.

50 D. J. Collins, B. Morahan, J. Garcia-Bustos, C. Doerig, M. Plebanski and A. Neild, *Nat. Commun.*, 2015, **6**, 8686.

51 S. Yang, Z. Tian, Z. Wang, J. Rufo, P. Li, J. Mai, J. Xia, H. Bachman, P.-H. Huang, M. Wu, C. Chen, L. P. Lee and T. J. Huang, *Nat. Mater.*, 2022, **21**, 540–546.

52 J. Li, L. Bo, T. Li, P. Zhao, Y. Du, B. Cai, L. Shen, W. Sun, W. Zhou and Z. Tian, *Adv. Mater. Technol.*, 2024, **9**(23), 2400572.

53 C. T. Presley, F. G. Vasquez and B. Raeymaekers, *Adv. Funct. Mater.*, 2024, **34**(33), 2400193.

54 M. Caleap and B. W. Drinkwater, *Proc. Natl. Acad. Sci. U. S. A.*, 2014, **111**, 6226–6230.

55 P. Kang, Z. Tian, S. Yang, W. Yu, H. Zhu, H. Bachman, S. Zhao, P. Zhang, Z. Wang, R. Zhong and T. J. Huang, *Lab Chip*, 2020, **20**, 987–994.

56 Z. Ma, A. W. Holle, K. Melde, T. Qiu, K. Poeppel, V. M. Kadiri and P. Fischer, *Adv. Mater.*, 2019, **32**, e1904181.

57 Y. Gu, C. Chen, J. Rufo, C. Shen, Z. Wang, P.-H. Huang, H. Fu, P. Zhang, S. A. Cummer, Z. Tian and T. J. Huang, *ACS Nano*, 2020, **14**, 14635–14645.

58 D. Wu, D. Baresch, C. Cook, Z. Ma, M. Duan, D. Malounda, D. Maresca, M. P. Abundo, J. Lee, S. Shivaei, D. R. Mittelstein, T. Qiu, P. Fischer and M. G. Shapiro, *Sci. Adv.*, 2023, **9**, eadd9186.

59 K. Melde, H. Kremer, M. Shi, S. Seneca, C. Frey, I. Platzman, C. Degel, D. Schmitt, B. Schölkopf and P. Fischer, *Sci. Adv.*, 2023, **9**, eadf6182.

60 M. Xu, C. Vidler, J. Wang, X. Chen, Z. Pan, W. S. Harley, P. V. S. Lee and D. J. Collins, *Small*, 2024, **20**, e2307529.

61 M. Baudoin, J.-C. Gerbedoen, A. Riaud, O. B. Matar, N. Smagin and J.-L. Thomas, *Sci. Adv.*, 2019, **5**, eaav1967.

62 M. Baudoin, J.-L. Thomas, R. A. Sahely, J.-C. Gerbedoen, Z. Gong, A. Sivery, O. B. Matar, N. Smagin, P. Favreau and A. Vlandas, *Nat. Commun.*, 2020, **11**, 4244.

63 X. Jiang, Y. Li, B. Liang, J. Cheng and L. Zhang, *Phys. Rev. Lett.*, 2016, **117**, 034301.

64 L. Zhang and P. L. Marston, *Phys. Rev. E: Stat., Nonlinear, Soft Matter Phys.*, 2011, **84**, 065601.

65 Z. Gong, P. L. Marston and W. Li, *Phys. Rev. Appl.*, 2019, **11**, 064022.

66 L. Zhang and P. L. Marston, *Phys. Rev. E: Stat., Nonlinear, Soft Matter Phys.*, 2011, **84**, 035601.

67 C. A. MacRae and R. T. Peterson, *Nat. Rev. Drug Discovery*, 2015, **14**, 721–731.

68 M. Ma, A. D. Ramirez, T. Wang, R. L. Roberts, K. E. Harmon, D. Schoppik, A. Sharma, C. Kuang, S. L. Goei, J. A. Gagnon, S. Zimmerman, S. Q. Tsai, D. Reyon, J. K. Joung, E. R. F. Aksay, A. F. Schier and Y. A. Pan, *J. Neurosci.*, 2019, **40**, 143–158.